

In Situ Polymerization of Aniline Derivative *in Vivo* for NIR-II Phototheranostics of Tumor

Aihui Wang,[†] Hongyan Li,[†] Hao Feng,[†] Huimin Qiu, Rimei Huang, Yiqin Wang, Shichen Ji, Hong Liang, Xing-Can Shen, and Bang-Ping Jiang*



Cite This: <https://doi.org/10.1021/acsami.2c19927>



Read Online

ACCESS |

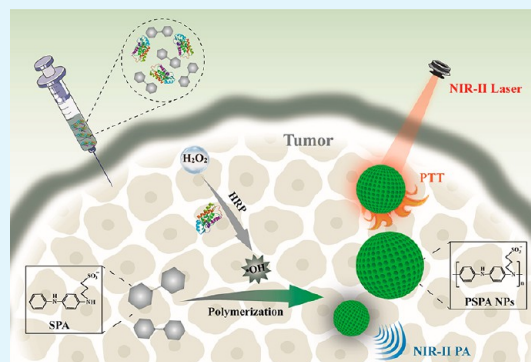
Metrics & More

Article Recommendations

Supporting Information

ABSTRACT: Natural biopolymers can be controllably *in situ* synthesized in organisms and play important roles in biological activities. Inspired by this, the manipulation of *in situ* biosynthesis of functional polymers *in vivo* will be an important way to obtain materials for meeting biological requirements. Herein, *in situ* biosynthesis of functional conjugated polymer at the tumor site was achieved via the utilization of specific tumor microenvironment (TME) characteristics for the first time. Specially, a water-soluble aniline dimer derivative (*N*-(3-sulfopropyl) *p*-aminodiphenylamine, SPA) was artfully *in situ* polymerized into polySPA (PSPA) nanoparticles at the tumor site, which was activated via the catalysis of hydrogen peroxide (H_2O_2) overexpressed in TME to produce hydroxyl radical ($\bullet OH$) by coinjected horseradish peroxidase (HRP). Benefiting from outstanding near-infrared (NIR)-II absorption of PSPA, the *in situ* polymerization process can be validly monitored by photoacoustic (PA) signal at the NIR-II region. Meanwhile, *in situ* polymerization would induce the size of polymeric materials from small to large, improving the distribution and retention of PSPA at the tumor site. On the combination of NIR-II absorption of PSPA and the size variation induced by polymerization, such polymerization can be applied for tumor-specific NIR-II light mediated PA image and photothermal inhibition of tumors, enhancing the precision and efficacy of tumor phototheranostics. Therefore, the present work opens the way to manipulate TME-activated *in situ* biosynthesis of functional conjugated polymer at the tumor site for overcoming formidable challenges in tumor theranostics.

KEYWORDS: *in situ* polymerization, tumor microenvironment, NIR II, tumor-specific phototheranostics, polyaniline derivative



1. INTRODUCTION

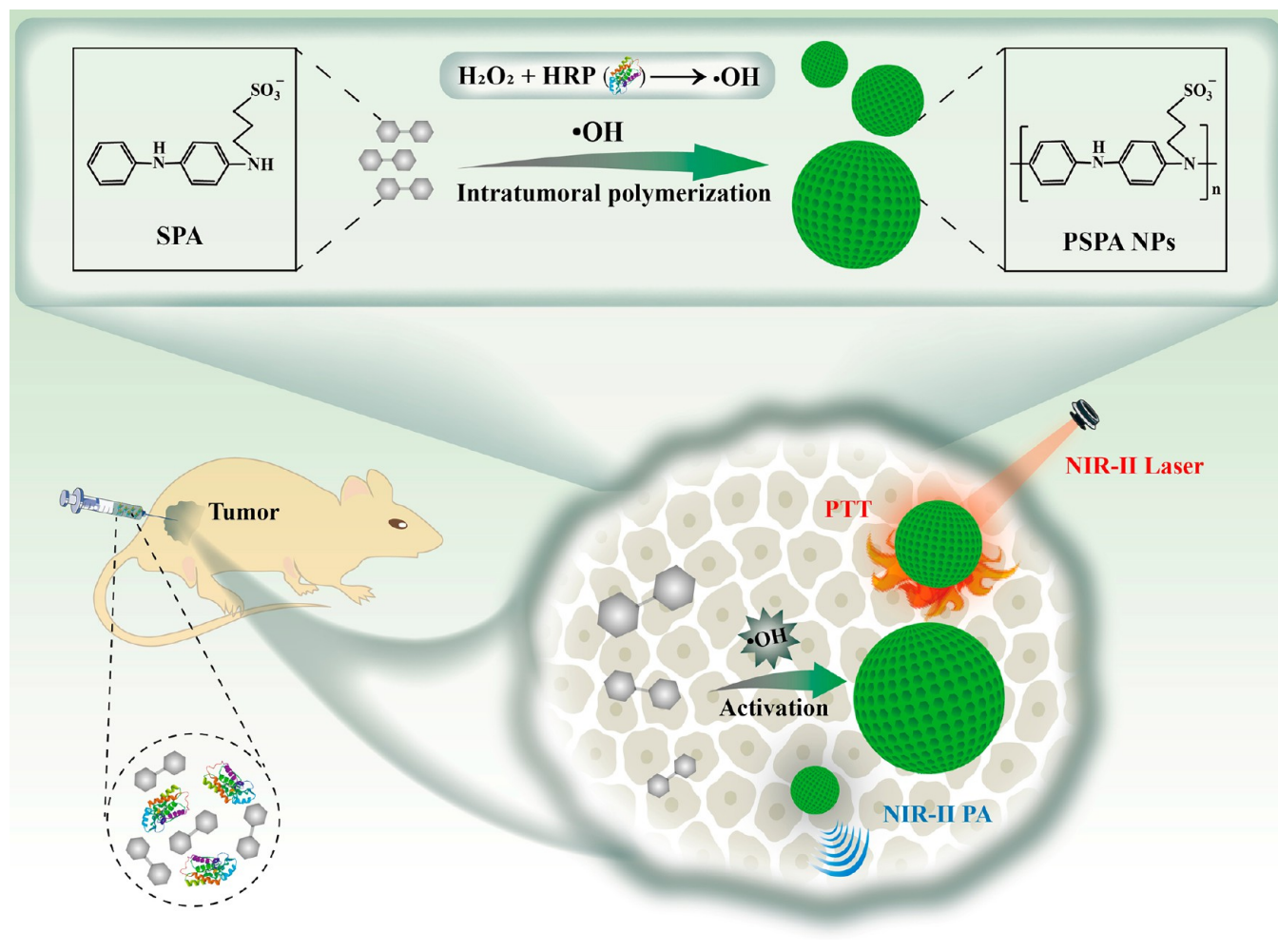
In nature, a series of biopolymers, such as polysaccharides and melanin, are controllably synthesized in organisms and play important roles in biological activities.¹ Inspired by this, artificial manipulation *in vivo* of *in situ* polymerization will be a greatly important way to obtain materials that meet biological needs.² Unfortunately, because of the harsh conditions of polymeric synthesis and the mild biological microenvironment, artificial manipulation *in vivo* of polymerization is still very challenging. Along this line, Berggren and Stavrinidou recently performed the seminal work to demonstrate that the spontaneous *in vivo* biosynthesis of conjugated polymers could happen in living organisms through electrical or biological-microenvironment activation, and the resultant polymers could be used to regulate biological functions.^{3–9} When considering the diverse functionalities and wide existence in organisms of biopolymers, successful manipulation of *in vivo* polymerization will be beneficial to not only meet biological needs, but also understand the fundamental processes of biosynthesis of biopolymers involved in organisms.^{3,5–7}

The malignant tumor is considered to be one of the biggest unsolved mysteries in the world,^{10–12} which has specific tumor microenvironment (TME) characteristics, including intratumoral hydrogen peroxide (H_2O_2) overproduction, intracellular glutathione (GSH) overproduction, mild acidic conditions, *etc.*^{13–17} It shows great potential to overcome the malignant tumor issues via the utilization of these TME characteristics to develop tumor-specific theranostic systems. For instance, acidic TME and specific enzymes were employed to switch size and surface charge of nanotheranostics;^{18–21} GSH and H_2O_2 were designed to activate change in the near-infrared (NIR) absorption of nanotheranostics.^{22,23} Nevertheless, there is still little research on the utilization of TME-activated *in situ* polymerization to enhance the precision and efficacy of tumor theranostics. In comparison to polymeric

Received: November 5, 2022

Accepted: January 4, 2023

Scheme 1. Schematic Illustration of *in Situ* Polymerization of SPA at the Tumor Site and Its Application for Tumor-Specific NIR-II Light Mediated PA Imaging and Photothermal Inhibition of Tumors



materials, small molecules possess several key advantages for tumor theranostics: efficient tissue distribution, deep penetration, and fast systemic clearance in normal tissues.^{24,25} However, they also suffer from poor retention compared to polymeric materials. *In situ* polymerization of small molecules into large polymers at the tumor site can take advantage of the efficient distribution and clearance of small molecules as well as the enhanced retention of polymeric materials. Among various kinds of polymers, conjugated polymers have tunable optical properties from visible to NIR-II light and good biocompatibility, which have achieved great advances in the field of tumor theranostics over the past decade.^{26–29} TME-activated *in situ* biosynthesis of conjugate polymers may offer the possibility to simultaneously regulate pharmacokinetic behaviors and theranostic performances via the adjustment of optical properties.^{30–33} Thereby, it is very meaningful to realize TME-activated *in situ* biosynthesis of conjugated polymers for tumor-specific theranostics.

Based on these understandings, we herein attempted to develop *in situ* biosynthesis of functional conjugated polymer at the tumor site via the utilization of specific TME characteristics for the first time, and further, the resultant polymerized material would be applied for realizing tumor-specific theranostics. In this system, H_2O_2 , which has been proved to be overexpressed in the tumor tissue (about $100 \mu\text{M}$),^{34–36} was chosen as an endogenous activated factor.

Horseshoe peroxidase (HRP), coinjected with polymeric monomer, was employed for catalyzing endogenous H_2O_2 to produce hydroxyl radical ($\cdot\text{OH}$), and it has been already proved that $\cdot\text{OH}$ can activate polymerization of conjugate monomer.^{37,38} When considering that polyaniline and its derivatives have good NIR absorption features as well as having been widely used in the field of tumor theranostics,^{26,39,40} a water-soluble and easily polymerizable aniline dimer derivative, *N*-(3-sulfopropyl) *p*-aminodiphenylamine (SPA), was selected as polymeric monomer to *in situ* biosynthesize polySPA (PSPA) nanoparticles (NPs) activated by $\cdot\text{OH}$ at the tumor site. *In situ* polymerized PSPA would generate NIR-II absorption, which can be used to effectively monitor the polymerization process by photoacoustic (PA) signal at NIR-II region. Meanwhile, *in situ* polymerization would induce the size variation of polymeric materials from small to large, improving the distribution and retention of PSPA at the tumor site. On the combination of NIR-II absorption of PSPA and the size variation induced by polymerization, such polymerization can be applied for tumor-specific NIR-II light mediated PA imaging and photothermal inhibition of tumors. With these distinguishing characteristics taken together, our TME-activated *in situ* polymerization of SPA to produce PSPA NPs will be the first example to utilize *in situ* biosynthesis of functional conjugated polymers at the tumor site for overcoming

formidable challenges in tumor theranostics. Specially, the precision and efficacy of tumor phototheranostics are artfully combined via the utilization of TME-activated *in situ* polymerization of water-soluble aniline derivative (Scheme 1).

2. EXPERIMENTAL SECTION

2.1. Materials and Reagents. All chemicals used are reagent grade unless noted. Horseradish peroxidase (HRP), dimethyl sulfoxide (DMSO), *N*-phenyl-*p*-phenylenediamine, and 1,3-propane sultone were purchased from Aladdin (Shanghai, China) Biochemical Technology Co., Ltd. Acetone, *N,N*-dimethylformamide (DMF), potassium bromide, formaldehyde (40%), and hydrogen peroxide (H₂O₂, 30%) were purchased from Xilong (Guangdong, China) Chemical Co., Ltd. Penicillin–streptomycin, 3-(4,5-dimethylthiazol-2-yl)-2,5-diphenyltetrazolium bromide (MTT), and propidine iodide (PI) were purchased from Sigma-Aldrich (America). Calcein-AM was purchased from Baiying biology science and technology (Tianjin, China) Co., Ltd. Fetal calf serum, DMEM medium, 1640 medium were purchased from HyClone (America). Mouse breast cancer cell (4T1) and human cervical carcinoma cells (HeLa) were purchased from Kunming Cell Bank, Chinese Academy of Sciences.

2.2. Preparation of SPA. The mixture of *N*-phenyl-*p*-phenylenediamine and 1,3-propane sultone as the molar mass ratio of 1:6 were reacted in a flask under N₂ environment for 6 h to obtain a blue solid. A proper amount of acetone was added to the obtained blue solid, and the solid was collected by vacuum filtration and dried. Then, an appropriate amount of secondary water was added into the obtained powder and filtered to obtain a blue aqueous solution; the blue solution was freeze-dried to obtain *N*-(3-sulfopropyl)-*p*-aminodiphenylamine (SPA) solid.

2.3. Characterizations and Instruments. Vis-NIR spectra were collected from 400 to 1200 nm by UV spectrophotometer (UV-2600, Shimadzu). Electron paramagnetic resonance (EPR) measurement was performed on Bruker A300. Gel permeation chromatography (GPC) data was obtained from Agilent PL-GPC50. Photothermal imaging was performed using an infrared thermal imager (MAG30, Magnity). Average size was measured on a laser particle size analyzer (Nano-ZS, Marven). Transmission electron microscope (TEM) images were obtained on a field transmission electron microscope (Talos 200S, ThermoFisher Scientific). Photoacoustic (PA) signal collected by a multispectral photoacoustic tomography system (inVision 256-TF, iThera Medical).

2.4. Cytotoxicity and Intracellular Polymerization. The cytotoxicity of SPA, SPA + HRP + H₂O₂, and PSPA was studied using 4T1 and HeLa cells as cell models by MTT assay. The 4T1 and HeLa cells in the logarithmic growth period were added to 96-well cell culture plates and incubated with SPA, SPA + HRP + H₂O₂, and PSPA for 24 h, respectively, and then, the standard MTT method was used to determine the survival rate of cells in each group. The absorbance was measured at 570 nm of each well using a 96-microwell plate reading with the absorbance at 630 nm as a reference. The cell survival rate was calculated by eq 1:

$$\text{Cell survival rate(\%)} = (\text{OD}_{\text{Experimental group}} / \text{OD}_{\text{Ctrl group}}) \times 100\% \quad (1)$$

Next, the polymerization of SPA into PSPA was studied in cells. 4T1 and HeLa cells were incubated with SPA and SPA + HRP + H₂O₂, respectively. Then, the PA imaging performance of each group was tested in the NIR-I (810 nm) and NIR-II (1065 nm) window. In addition, EPR signals of each group were collected by electron paramagnetic resonance spectrometer.

TEM cell samples were fixed with glutaraldehyde for 2 h and then dehydrated with 10%, 30%, 50%, 70%, 90%, and 100% ethanol gradient, respectively. After the cells were embedded in sections, they were stained with uranyl acetate and lead citrate, respectively, and TEM images were obtained by field transmission electron microscope.

2.5. In Vitro Phototheranostics. To evaluate the effect of phototherapy *in vitro*, we synthesized *d*-PSPA in the presence of H₂O₂ (100 μM) and HRP (0.2 mg mL⁻¹) for 6 h. In addition, 4T1 and

HeLa cells in each laser-irradiated (1064 nm, 1.0 W cm⁻², 5 min) group were stained with Calcein-AM and PI after 24 h incubation. Calcein-AM is a kind of green fluorescent dye which can be used to label living cells, and PI is a kind of red fluorescent dye which can be used to label dead cells. Combination of the two fluorescent dyes can simultaneously detect the living and dead cells under the confocal laser scanning microscope (CLSM, Leica, TCS SP8 DIVE).

2.6. In Situ Polymerization in Tumor Tissue. 4T1 tumor-bearing female Balb/c nude mice were selected as an animal model. All *in vivo* experiments concerning animals had strictly referred to the experimental manipulations performed on living vertebrates and were under the supervision of the Ethics Committee of Guangxi Normal University Laboratory Animal Centre, as well as authorized by it. The assigned approval accreditation number of this work is 202209–02. After tumor sizes grew to ≈100 mm³, mice were intratumorally injected with SPA and SPA + HRP, respectively. As a control, normal tissues were injected with SPA + HRP. The variation of PA signal at 1065 nm was continuously monitored in the tumor site within 48 h after the injection.

In order to further explore the *in situ* polymerization of PSPA in the tumor tissue, tumor tissues were collected 24 h after SPA + HRP injection. The tumor tissues were fixed with glutaraldehyde for 2 h and then dehydrated with 10%, 30%, 50%, 70%, 90%, and 100% ethanol gradient, respectively. After the tumor tissue were embedded in sections, they were stained with uranyl acetate and lead citrate, respectively, and TEM images were obtained by field transmission electron microscope. When considering that the excellent conductivity of the polyaniline skeletons of PSPA, SPA, and SPA + HRP was injected into tumor tissues, after 24 h, the tumor tissues were peeled off and the electrical conductivity of tumors in each treatment group was measured.

2.7. In Vivo Phototheranostics. In order to evaluate the PTT effect *in vivo*, 4T1 tumor-bearing mice were randomly divided into 8 groups (5 mice in each group). Specifically, saline, SPA (3.5 mg mL⁻¹), *d*-PSPA (3.5 mg mL⁻¹), and SPA + HRP (contains 0.2 mg mL⁻¹ HRP and 3.5 mg mL⁻¹ SPA) were injected into tumor sites of tumor-bearing mice in different experimental groups at 100 μL, respectively. After 12 h of injection, the tumor was irradiated with or without 1064 nm laser (1.0 W cm⁻²) for 10 min. During this period, the photothermal process was monitored by infrared cameras. Furthermore, the daily tumor volume and weight changes of mice were recorded. The tumor volume was calculated by eq 2:

$$V = (a \times b^2) / 2 \quad (2)$$

In the equation, *a* represents tumor length; *b* represents tumor width.

The relative tumor volume was calculated by eq 3:

$$\text{Relative tumor volume} = V / V_0 \quad (3)$$

In the equation, *V*₀ represents the initial tumor volume before the start of treatment (day 0).

All results were expressed as means ± standard error of mean (SEM) and analyzed using GraphPad Prism 9 or Origin 2021. Statistically significant differences were assessed by unpaired Student's *t* test for two groups, one- or two-way analysis of variance (ANOVA) for multiple groups, or Log-rank test for survival analysis in GraphPad software, unless noted exceptionally. *P* values <0.05 were considered statistically significant (**p* < 0.05, ***p* < 0.01, ****p* < 0.001, and *****p* < 0.0001).

2.8. Histology Evaluation. For histological evaluation, the tumor tissue, heart, liver, spleen, lung, and kidney organ samples of each treatment group were collected on the 14th day after treatment. The collected specimens were immediately fixed in 4% formaldehyde and subsequently embedded in paraffin for sectioning. Organ and tumor specimens were stained with hematoxylin and eosin (H&E), stained histological sections were observed under an automatic cell imaging system (EVOS FL Auto 2, ThermoFisher Scientific).

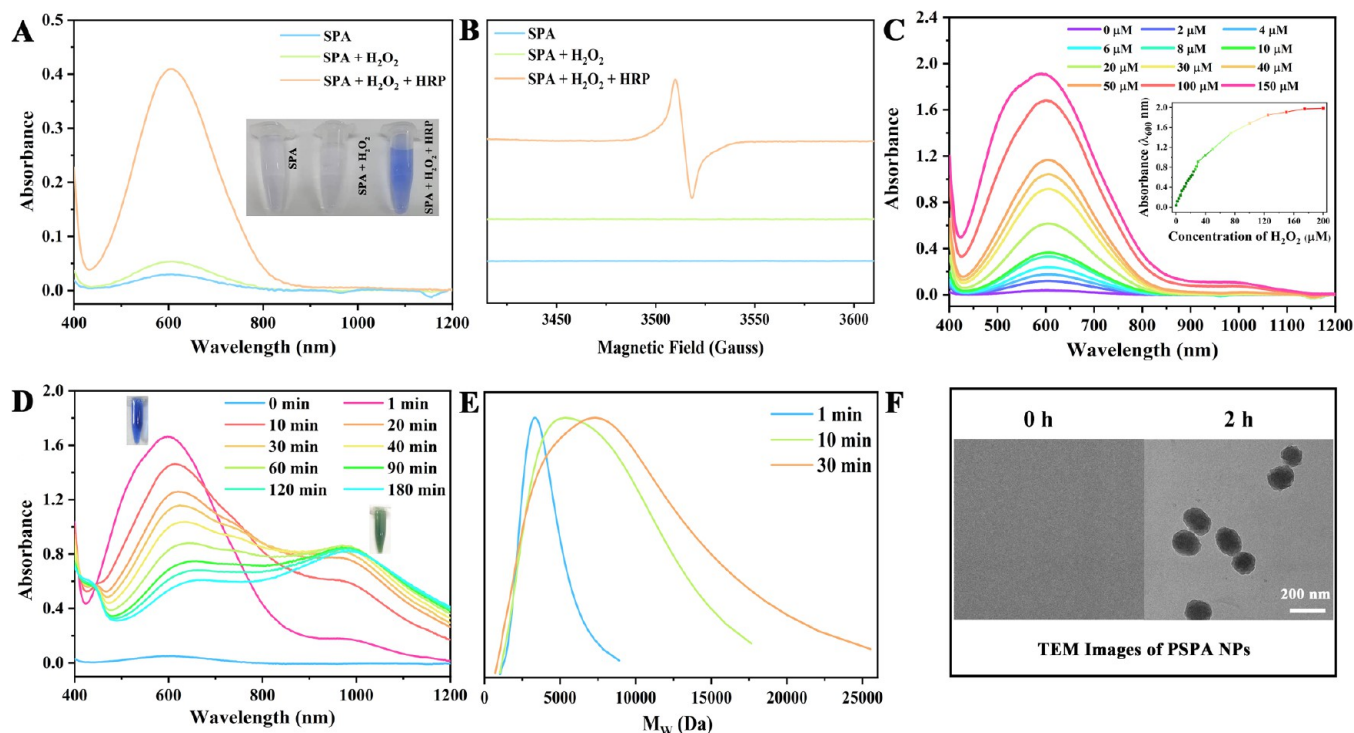


Figure 1. (A) Vis-NIR spectra of SPA, SPA + H₂O₂, and SPA + H₂O₂ + HRP. (B) EPR signals of SPA, SPA + H₂O₂, and SPA + H₂O₂ + HRP. (C) Vis-NIR spectra of SPA treated with fixed HRP and different H₂O₂ concentrations. Inset in (C): H₂O₂ concentration-dependent absorption (600 nm) curve. (D) Time-dependent Vis-NIR spectra of SPA in the presence of HRP and H₂O₂ (100 μM). (E) Time-dependent gel permeation chromatography test. (F) TEM images of SPA after the polymerization for 0 and 2 h. Scale bar: 200 nm.

3. RESULTS AND DISCUSSION

3.1. H₂O₂-Responsive Polymerization Behavior of SPA

With the aim of obtaining water-soluble aniline derivatives, we first prepared SPA via the reaction of *N*-phenyl-*p*-phenylenediamine and 1,3-propane sultone according to the previous work.^{41,42} The solubility of SPA was tested, which was found to exhibit high solubility in various mediums, including deionized water, phosphate-buffered saline (PBS), saline, DMEM medium, and 1640 medium (Figure S1). Subsequently, the polymerization of SPA was studied in the presence of HRP and H₂O₂. In general, the polymerization of aniline derivatives to produce a polyaniline skeleton would be accompanied by the absorption spectrum transformation.^{41,43} The absorption spectra of SPA with the treatment of HRP and H₂O₂ were measured by visible-near-infrared (Vis-NIR) absorption spectrometry. As shown in Figure 1A, SPA aqueous solution showed no obvious absorption peak at about 600 nm. However, absorbance ranging from 500 to 800 nm, assigned to characteristic absorption of polyaniline skeleton, immediately appeared after the addition of HRP and H₂O₂. It can also be intuitively observed that the solution color varied from colorless to blue (Figure 1A, inset). As a control, the absorption spectrum was also obtained for SPA after treatment only with H₂O₂, and insignificant characteristic absorption of polyaniline skeleton was found. To prove the polymerization of SPA to produce a polyaniline skeleton, the electron paramagnetic resonance (EPR) measurement was carried out. Intrinsic EPR signal of the polyaniline skeleton was found for SPA after being treated with HRP and H₂O₂, whereas insignificant EPR signal was observed for only SPA and SPA after being treated with H₂O₂ (Figure 1B). These observations indicated that the simultaneous existence of HRP and H₂O₂ is

a necessary condition for the polymerization of SPA to produce PSPA. When considering that HRP can catalyze H₂O₂ to produce •OH and •OH which has been proved to initiate the polymerization of aniline derivatives,³⁰ we can infer that •OH produced from the catalysis of H₂O₂ by HRP activated the polymerization of SPA.

To further explore that •OH activated the polymerization of SPA, Vis-NIR absorption variations of SPA after treatment with HRP and H₂O₂ were investigated at different H₂O₂ concentrations and reaction times. Compared with the normal tissue, tumor tissue has overexpressed H₂O₂, but the expression level of H₂O₂ is usually limited (about 100 μM),^{34–36} which greatly restricted the occurrence of oxidative polymerization initiated by H₂O₂. We primarily explored the H₂O₂ responsiveness of this polymerization at different H₂O₂ concentrations. The absorption intensity around 600 nm gradually rose with the increase of H₂O₂ concentrations in the range from 2 to 150 μM (Figure 1C), and SPA can even respond to the H₂O₂ concentration as low as 2 μM, exhibiting high responsive sensitivity of the polymerization of SPA to H₂O₂. It should be noted that such high responsive sensitivity of the polymerization will provide the enormous possibility for the subsequent use of H₂O₂ overexpressed in the TME to realize the *in situ* polymerization of SPA. As shown in Figure 1D, with the extension of reaction time, the characteristic absorption peak centered around 600 nm had significant red shift, and meanwhile, another new absorption peak appeared near 1000 nm, accompanying the solution color change from blue to green (Figure 1D, inset). Subsequently, pH-dependent vis-NIR measurement of polymeric solutions was performed. As shown in Figure S2, the absorption peak at 1000 nm gradually disappeared upon the increase in pH values, and the colors of the solutions changed from green to blue. Combining

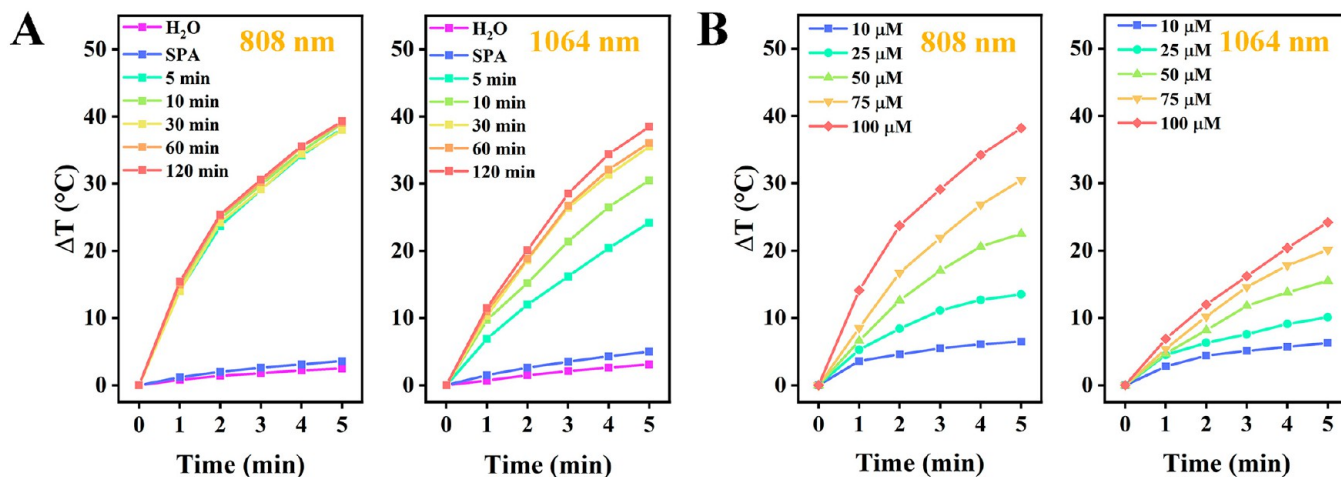
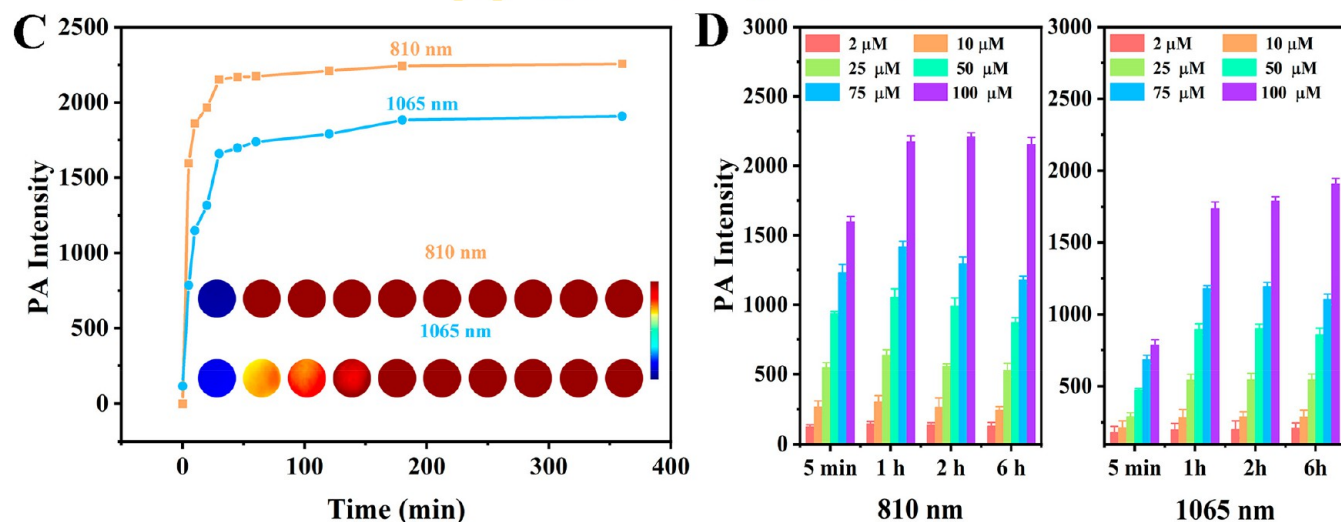
H_2O_2 -responsive photothermal performances H_2O_2 -responsive PA performances

Figure 2. (A) Time-dependent photothermal curve of SPA samples after polymerization for different times. The polymerization was performed with H_2O_2 ($100 \mu\text{M}$) in the presence of fixed HRP (0.2 mg mL^{-1}). (B) Time-dependent photothermal curve of SPA treated with different concentrations of H_2O_2 in the presence of fixed HRP. The laser irradiation in (A) and (B) was performed using 808 and 1064 nm laser (1.0 W cm^{-2}). (C) Time-dependent PA signal curves at 810 and 1065 nm of SPA after treatment with H_2O_2 ($100 \mu\text{M}$) in the presence of fixed HRP. Inset in (C): their corresponding PA photographs. (D) PA intensities at 810 and 1065 nm of SPA after treated with different concentrations of H_2O_2 in the presence of fixed HRP. All data are presented as mean \pm SD ($n = 3$).

the previous studies on absorption properties of polyaniline derivatives,^{41,44} the absorption peak near 1000 nm was assigned to emeraldine salt resulting from doping the proton of $-\text{SO}_3\text{H}$ into the polyaniline skeleton, causing the movement of electrons and decreasing the excitation-energy level. In addition, the absorption peak centered around 600 nm corresponded to the quinoid ring of the polyaniline skeleton. With an increase in the pH, the emeraldine salt was transformed into an emeraldine base, and the characteristic absorption near 1000 nm of the emeraldine salt gradually disappeared. To further verify the polymerization of SPA, the samples were characterized by FT-IR spectroscopy. As shown in Figure S3, the two strong vibrations in the SPA at 1597 and 1515 cm^{-1} were assigned to symmetric ($\text{C}=\text{C}$) and antisymmetric ($\text{C}=\text{C}$) stretching, and they shifted to 1594 and 1511 cm^{-1} in the PSPA. Combining the previous studies on FT-IR properties of polyaniline derivatives,^{45,46} such

vibrational shift could be ascribed to the polymerization of SPA to form the polyaniline skeleton. In addition, a peak appeared at 1158 cm^{-1} assigned to the stretching vibration of $-\text{NH}^+=$ structure in the doped PSPA. These results proved that SPA could be polymerized to produce PSPA in the presence of HRP and H_2O_2 . Time-dependent gel permeation chromatography (GPC) measurement was also performed to explore the molecular weight of PSPA at different polymerization times (Figure 1E). The time-dependent GPC result revealed that the polymerization of SPA can rapidly occur, and the molecular weight of PSPA gradually increased with the extension of polymerization time, which well agreed with the vis-NIR absorption result. After those, dynamic light scattering (DLS) and transmission electron microscopy (TEM) measurements were employed to characterize size and morphology variations before and after the polymerization. DLS data displayed that the average hydrodynamic diameter was about

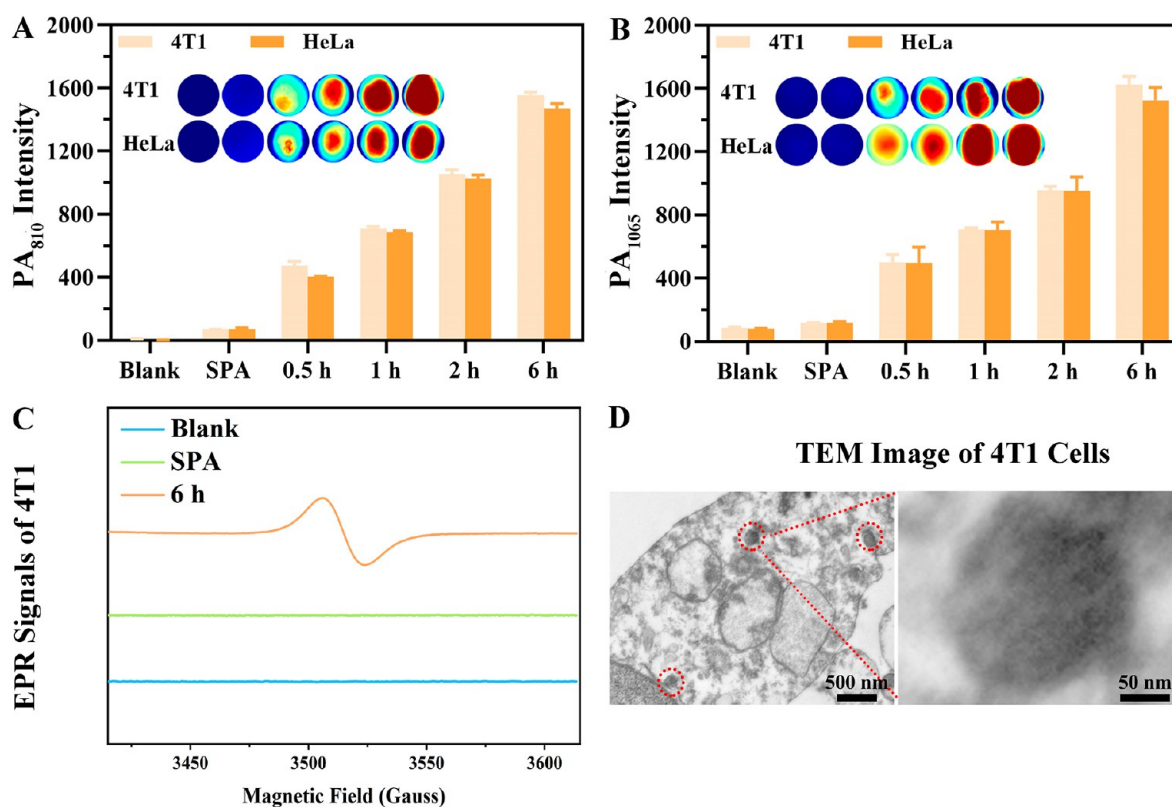


Figure 3. *In vitro* PA signal intensities at 810 nm (A) and 1065 nm (B) of 4T1 and HeLa cells after treatment with H₂O₂ (100 μM) for different times in the presence of fixed HRP. Inset in (A) and (B): their corresponding PA photographs. (C) EPR signals of 4T1 cells in different treatment groups. (D) TEM image of as-polymerized PSPA NPs in 4T1 cells. Red dashed circles were used to label NPs. Scale bar: 500 nm. Inset: Enlarged view of NPs. Scale bar: 50 nm. All data are presented as mean ± SD (*n* = 3).

200 nm after the polymerization, while an insignificant DLS signal was found before the polymerization (Figure S4). The TEM measurement implied that the polymerization of SPA led to the generation of 150–200 nm spherical nanoparticles, whereas no obvious specific morphology was found for SPA before the polymerization (Figure 1F). Such size variation (small to large) and nanosized morphology are both suited for further biomedical applications.

3.2. H₂O₂-Responsive Photothermal and PA Performances. The excellent NIR-I and NIR-II absorption feature may endow the polymerization of SPA to be applied for NIR light mediated phototheranostics, including PA imaging and phototherapy.^{28,47,48} The photothermal conversion behavior of the *in situ* polymerized PSPA was primarily studied under irradiation using two lasers with different wavelengths (808 and 1064 nm). The aqueous solution obtained from the polymerization of SPA at different time points was irradiated with NIR-I light (808 nm, 1.0 W cm⁻²) and NIR-II light (1064 nm, 1.0 W cm⁻²) for 5 min. When considering that the concentration of H₂O₂ in the TME is generally about 100 μM, 100 μM was herein used to activate the polymerization of SPA. According to Figure 2A, even after the polymerization of SPA happened for 5 min, the temperature of the corresponding solution can be increased by over 25 °C whether irradiated by 808 nm laser or 1064 nm laser, which is enough to be used for damaging tumor cells. In addition, the SPA aqueous solution irradiated by 808 and 1064 nm lasers showed different polymerization time-dependent temperature change behaviors. Under 808 nm laser irradiation, no obvious polymerization time-dependent temperature change was found, whereas under 1064 nm laser

irradiation, the temperature elevation of the resultant solution gradually became more prominent as the polymerization time increased. Such polymerization time-dependent temperature change under 1064 nm laser irradiation can be ascribed to the enhancement of NIR-II absorbance induced by more doping and the formation of high molecular weight PSPA upon the increase of polymerization time, in according with polymerization time-dependent Vis-NIR absorption results (Figure 1D). As a control, the temperature of pure water and the SPA solution showed no obvious heating phenomenon under the same condition (Figures 2A and S5). This result indicated that PSPA obtained from the polymerization of SPA can efficiently convert the NIR-I and II light into heat. As shown in Figure S6, the photothermal conversion efficiencies (PCE) of the solutions obtained after 2 h of polymerizations were 40.35% for 808 nm laser irradiation and 42.90% for 1064 nm laser irradiation using the data obtained from Figure 2A. These values are comparable to those of other already reported conjugated polymers.^{40,47}

Furthermore, the photothermal behaviors of the solution after the polymerization for 5 min were investigated with different amounts of H₂O₂ under 808 and 1064 nm laser irradiation, respectively. As shown in Figure 2B, the photothermal conversion ability of the polymerization solution is dependent on the concentration of H₂O₂, and even at low-concentration H₂O₂ (25 μM), the polymerization solution could still be heated by 13.5 and 10.1 °C upon both 808 and 1064 nm laser irradiation, indicating excellent photothermal conversion capability. Meanwhile, cyclic irradiation experiment was performed (Figure S7). The temperature variation of

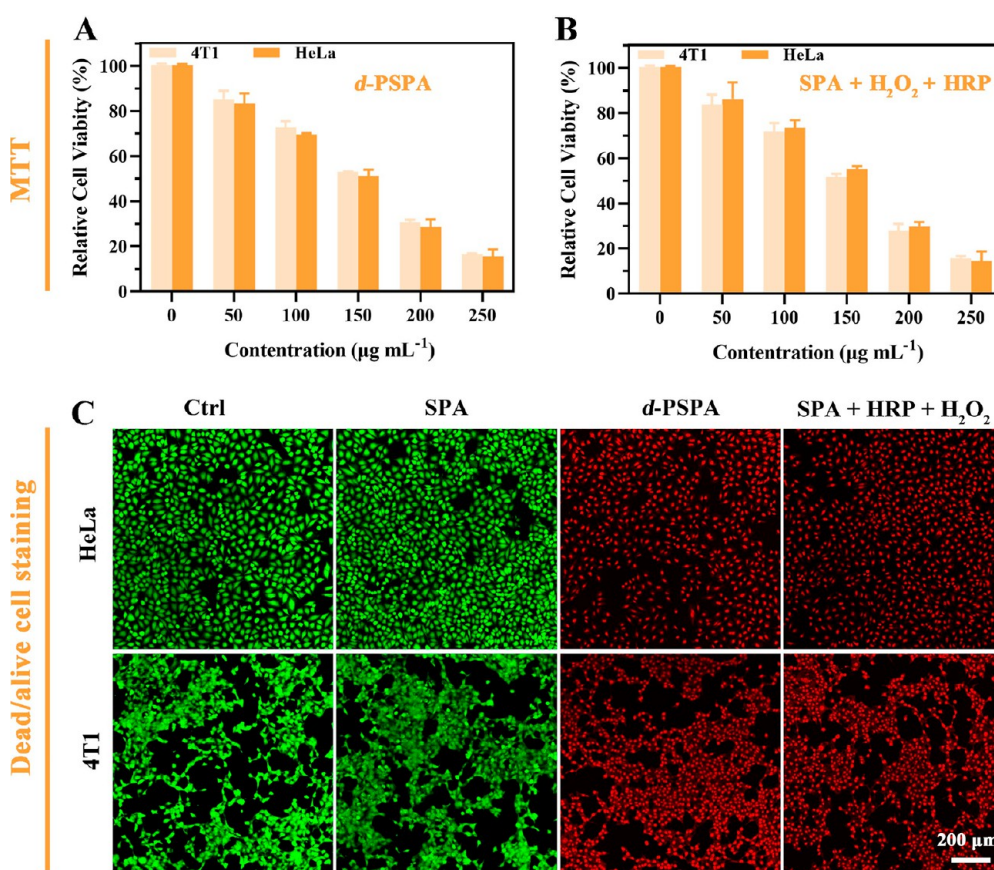


Figure 4. Concentration-dependent *in vitro* photothermal-induced cell-killing effect of 4T1 and HeLa cells: *d*-PSPA (A) and SPA in the presence of fixed HRP and H₂O₂ (100 μM) (B). (C) Confocal laser scanning microscopy images of 4T1 and HeLa cells stained with calcein-AM (green, living cells) and propidium iodide (red, dead cells) after different treatments, respectively. The laser irradiation was performed using 1064 nm laser (1.0 W cm^{-2}). Scale bar: 200 μm . All data are presented as mean \pm SD ($n = 3$).

polymerization solution showed insignificant deterioration after repeated heating/cooling processes under 808 and 1064 nm laser irradiation, implying good photothermal stability of PSPA. These results indicated that SPA could be polymerized to PSPA with remarkable photothermal capability in the presence of HRP and H₂O₂ (100 μM), which would have the potential to be applied for tumor-specific PTT via ROS activation.

In addition to the possibility of NIR-light mediated PTT, the polymerization of SPA into PSPA may be applied for NIR-light mediated PA imaging.^{18,32,47} PA imaging behavior of SPA solution was evaluated in the presence of HRP and H₂O₂ for different times (Figure 2C). As the polymerization time increased, the PA signal intensities at 810 and 1065 nm of the sample solution gradually rose. In contrast, the mixture of HRP and H₂O₂ displays insignificant PA signals at 810 and 1065 nm (Figure S8), indicating that the obvious PA signal of the sample solution is mainly attributed to the polymerization of SPA into PSPA. PA signal variation of the polymerization process was also assessed in response to different concentrations of H₂O₂. As shown in Figure 2D, the PA signal intensities at 810 and 1065 nm increases significantly with the increase of H₂O₂ concentration, and the variation in the intensity of the PA signal is consistent with that the absorption spectra (Figure 1C). It should be mentioned that even at low-concentration H₂O₂ (25 μM), the sample solution still has a strong PA signal. When considering that it has 100 μM H₂O₂ in TME, it suggests that the polymerization of SPA into PSPA

has the potential to be used for *in situ* NIR-light mediated PA imaging of the tumor.

3.3. Intracellular Polymerization and *in Vitro* Phototheranostics. Before the study on the intracellular polymerization of SPA and the evaluation of the *in vitro* phototheranostics of PSPA, the *in vitro* biocompatibility of SPA and PSPA was primarily investigated via a standard MTT assay. Two kinds of cancer cells were chosen to assess the *in vitro* biocompatibility: mouse breast cancer (4T1) cells and human cervical carcinoma (HeLa) cells. The MTT assay result indicated that the cell viabilities of both 4T1 and HeLa cells remain more than 85% even at the highest concentration of 250 $\mu\text{g mL}^{-1}$ for SPA or PSPA in various groups, including SPA, SPA + HRP + H₂O₂ (HRP, 0.2 mg mL^{-1} ; H₂O₂, 100 μM), and PSPA (Figure S9). It revealed that the dark cytotoxicity of each group is negligible, as well as SPA and PSPA having good biocompatibility.

Next, the polymerization of SPA into PSPA was studied in cells. 4T1 and HeLa cells were incubated with SPA and SPA + HRP + H₂O₂, respectively. Then, the PA imaging performance of each group was tested in the NIR-I (810 nm) and NIR-II (1065 nm) windows. In the blank group (only treated by PBS) and SPA group, insignificant PA signal could be observed in the cell solution (Figure 3A and B). By contrast, significant PA signals at 810 and 1065 nm could both be observed in the SPA + HRP + H₂O₂ group (Figure 3A and B). Specifically, as the incubation time increased, the PA signal gradually increased. This observation agreed well with the PA imaging result

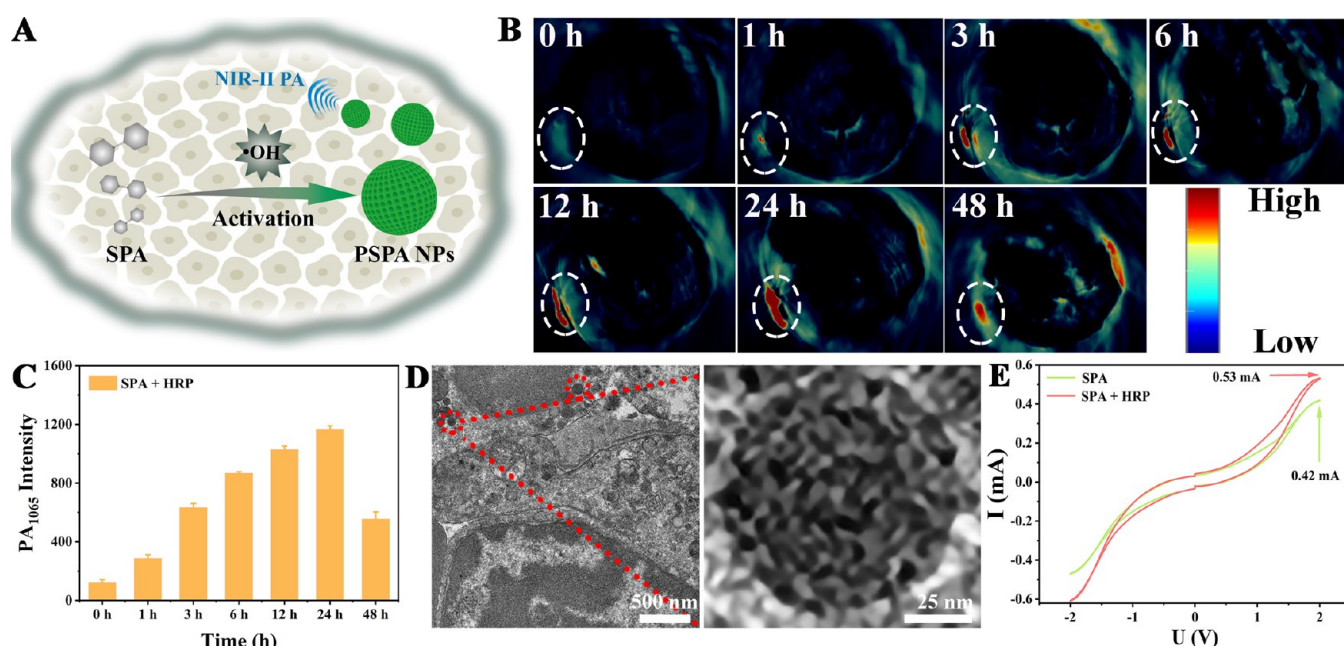


Figure 5. (A) Schematic illustration of *in situ* polymerization of SPA at tumor tissue initiated by $\bullet\text{OH}$ for PA imaging. (B) Time-dependent PA imaging and corresponding PA intensity (C) of 4T1 tumor-bearing mice intratumorally injected with SPA + HRP. (D) TEM image of polymerized PSPA NPs in 4T1 tumor tissue. Red dashed circles were used to label NPs. Scale bar: 500 nm. Inset: Enlarged view of NPs. Scale bar: 25 nm. (E) Electrical conductivity of tumor tissue injected with SPA and SPA + HRP. All data are presented as mean \pm SD ($n = 3$).

obtained from the polymerization of SPA in aqueous solution (Figure 2C), confirming that SPA could be effectively polymerized in the cells. EPR spectroscopy also proved the formation of PSPA in the cells. An obvious intrinsic EPR signal of the polyaniline skeleton was observed for the SPA + HRP + H_2O_2 group, whereas the EPR signal was not found for the blank group (only treated by PBS) or the SPA group (Figures 3C and S10). Moreover, TEM measurement was also used to further verify the formation of PSPA NPs in the cells. As shown in Figure 3D, after SPA + HRP + H_2O_2 incubation for 12 h, solid spherical NPs of 100–200 nm, differing from endogenous vesicles that have typical vesicle wall and show a hollow structure, could be observed in the 4T1 cells. As a control, no solid spherical NPs were observed in the untreated 4T1 cells (Figure S11). The NPs without the vesicle wall structure illustrated that they comprised highly conjugated polymer PSPA, resulting from the polymerization of SPA into PSPA NPs in the cells.

On the basis of these results, phototherapeutic efficacy was *in vitro* assessed. A 1064 nm laser (1.0 W cm^{-2}) was used to irradiate 4T1 and HeLa cells for 5 min. To demonstrate the feasibility of the *in situ* synthesized PSPA (the SPA + HRP + H_2O_2 group) via the polymerization of SPA for phototherapeutics, we selected the directly synthesized PSPA (denoted as *d*-PSPA) for comparison in such *in vitro* experiments. Specially, *d*-PSPA was synthesized by the reaction of SPA catalyzed by HRP (0.2 mg mL^{-1}) in the presence of H_2O_2 ($100 \mu\text{M}$) for 6 h. Before assessing phototherapeutic efficacy, we studied the interaction of *d*-PSPA and *in situ* synthesized PSPA with cells by PA signal. Insignificant difference of PA intensity was seen between cells treated by *d*-PSPA and those treated by *in situ* polymerized PSPA (Figure S12), indicating that both of them can effectively interact with cells via surface adsorption or internalization. With the increase in the concentration of the SPA unit, the cell viability was significantly reduced for both the SPA + HRP + H_2O_2 group

and *d*-PSPA group under laser irradiation (Figure 4A and B), and such a decrease in the cell viability is comparable between the two. At the highest concentration of $250 \mu\text{g mL}^{-1}$, the relative cell viability of 4T1 and HeLa cells dropped below 15%. As control, only SPA could not cause an obvious reduction in the cell viability under laser irradiation (Figure S13). These observations implied that the photoinduced cell killing of the SPA + HRP + H_2O_2 group was attributed to the *in situ* synthesized PSPA in the cells. Specifically, *in situ* synthesized PSPA produced heat to damage cells under 1064 nm laser irradiation. To visually evaluate the photothermal ablation of cancer cells induced by the *in situ* synthesized PSPA under laser irradiation, live and dead cells were stained with green emitting calcein-AM and red emitting propidium iodide, respectively (Figure 4C). Green fluorescence was clearly observed in the SPA group before and after 1064 nm laser irradiation (1 W cm^{-2}) for 5 min. In contrast, strong red fluorescence was clearly visible for the *d*-PSPA and SPA + HRP + H_2O_2 groups after laser irradiation for 5 min. Similar photoinduced cell killing behavior of the SPA + HRP + H_2O_2 group was also observed under 808 nm laser irradiation (Figure S14). These observations indicated that the *in situ* synthesized PSPA in cells exhibited both NIR-I and NIR-II light-mediated killing of cancer cells, favoring for subsequent *in vivo* PTT of cancer.

3.4. In Situ Polymerization and In Vivo Phototheranostics. Encouraged by desirable polymerization of SPA as well as PA and photothermal effects of the *in situ* synthesized PSPA in solution and *in vitro*, the polymerization behavior of SPA using H_2O_2 overexpressed in the TME and the phototheranostics property of the *in situ* synthesized PSPA were then *in vivo* assessed. 4T1 tumor-bearing female Balb/c nude mice were selected as the animal model. After tumor sizes grew to $\approx 100 \text{ mm}^3$, mice were intratumorally injected with SPA + HRP. When considering that NIR-II light has better tissue penetration,^{49–51} NIR-II light was used to perform

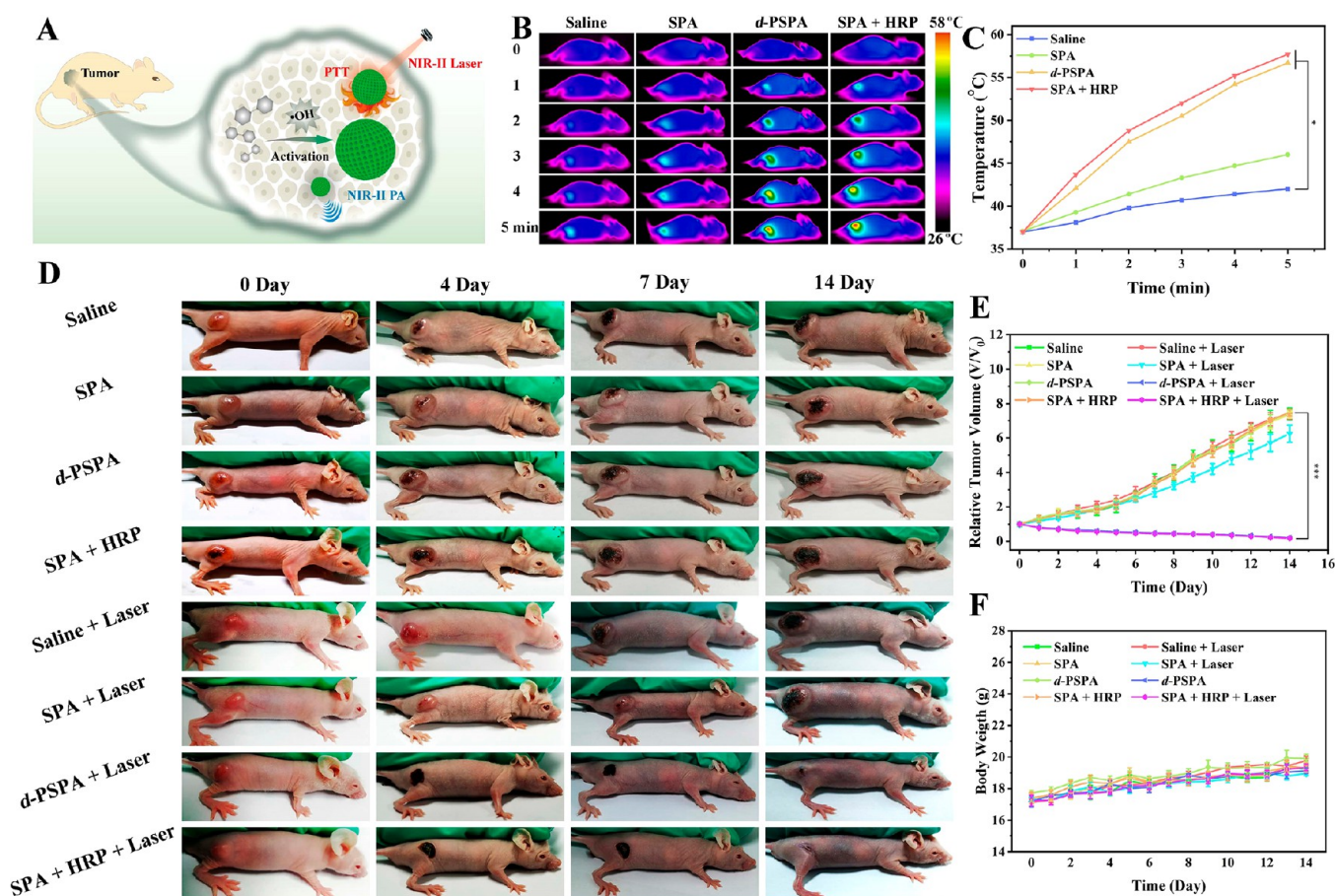


Figure 6. (A) Schematic illustration of *in situ* polymerization of SPA at tumor tissue initiated by $\bullet\text{OH}$. (B) Photothermal images of 4T1 tumor-bearing mice in different treatment groups. (C) The corresponding time-dependent photothermal curve displayed in (B). The irradiation was performed using 1064 nm laser (1.0 W cm^{-2}) for 5 min. (D) Photographs of 4T1 tumor-bearing mice after different treatments on days 0, 4, 7, and 14. Tumor growth curves (E) and weight change curves (F) of different treatment groups within 14 days. All data are presented as mean \pm SD ($n = 3$). *** $p < 0.001$; * $p < 0.05$.

subsequent phototheranostics *in vivo*. The variation of the PA signal at 1065 nm was continuously monitored at the tumor site within 48 h after the injection (Figure 5A). As could be seen from Figure S15, the PA signal at the tumor site of the SPA group did not change significantly throughout the whole period. However, the PA signal of the SPA + HRP group gradually increased during the first 24 h (Figure 5B and C). It reached the maximum intensity at about 24 h and gradually attenuated. This indicated that in the presence of the HRP, SPA can be *in situ* polymerized to form PSPA using H_2O_2 overexpressed at the tumor site. On the contrary, when SPA + HRP was injected into the normal tissue on the back of the mouse, insignificant PA signal at 1065 nm was found (Figure S16), attributed to the lack of H_2O_2 required for polymerization in normal tissues. Such a remarkable difference in PA intensity between tumor and normal tissues indicated that *in situ* polymerization of SPA can be used for tumor-specific PA imaging in the NIR-II region. In addition, time-dependent PA intensity was utilized to compare the polymerization differences of SPA in solution and in tumor tissue. As shown in Figure S17, we could find that PA intensity has almost remained unchanged for SPA in solution after 3 h treatment of HRP and $100 \mu\text{M H}_2\text{O}_2$, whereas for SPA in tumor tissues, PA intensity reached a plateau until 12 h. In addition, the PA intensity in the solution group was also higher than that in the tumor tissue group when the time-dependent PA intensity

reached a plateau. These results indicated that SPA polymerized faster and more effectively in solution than in tumor tissue, possibly because of lower switching speed and less fluid in tumor tissues than in solution, which reduce the *in situ* biosynthesis rate of PSPA. Furthermore, TEM measurement of tumor tissue was performed to verify the *in situ* polymerization of SPA to form PSPA NPs. As shown in the Figure 5D, solid spherical NPs with 100–200 nm, differing from endogenous vesicles that have typical vesicle wall and hollow structure, could be observed in the space between tumor tissues and tumor cells, after intratumoral injection of SPA + HRP for 12 h. As a control, no solid spherical NPs were observed in the untreated tumor tissues (Figure S18). Combining the aforementioned TEM results of *in situ* synthesized PSPA NPs in the cells, it can be inferred that these solid spherical NPs were PSPA NPs obtained by *in situ* polymerization of SPA at the tumor site. When considering that the polyaniline skeleton of PSPA is one kind of conducting polymer, the conductivity of the tumor treated by SPA was measured in the absence and presence of HRP (Figures 5E and S19). The tumor treated by SPA in the absence of HRP displayed a significant conductivity change compared to the tumor treated by SPA in the presence of HRP. In Figure 5E, the current intensity at 2 V increased from about 0.42 to 0.53 mA. Meanwhile, time-dependent current intensity displayed a similar phenomenon (Figure S19). Such variation in current

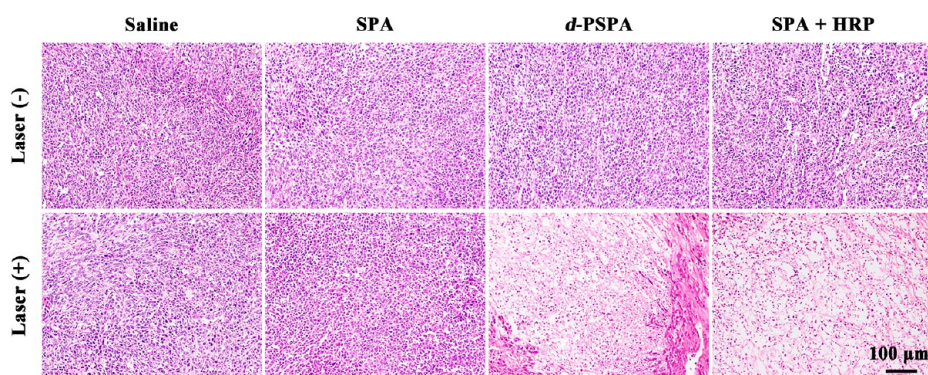


Figure 7. H&E staining of tumor tissue sections of 4T1 tumor-bearing mice after different treatments for 14 day. Scale bar: 100 μm .

intensity revealed the increase in the electron transfer, further proving that the conducting polyaniline skeleton was formed as a result of *in situ* polymerization of SPA into PSPA. These results indicated that SPA can be effectively *in situ* polymerized into PSPA at the tumor site through the utilization of HRP to catalyze H_2O_2 overexpressed in the TME, and such *in situ* synthesized PSPA NPs can be further applied for tumor-specific PA imaging in NIR-II region.

Based on the efficacious *in situ* polymerization of SPA into PSPA NPs at the tumor site, we attempted to further assess the corresponding photothermal behavior *in vivo* using the same tumor model as that used in PA imaging. According to the results of PA image *in vivo*, the tumor was irradiated using 1064 nm laser (1.0 W cm^{-2}) after 12 h of intratumoral injection of SPA and HRP (Figure 6A). The photothermal process was monitored by infrared cameras. As shown in Figure 6B, the tumor temperature of the *d*-PSPA group and the SPA + HRP group gradually increased from 37°C to over 50°C during irradiation for 5 min, comparable to each other. Such a noticeable rise in tumor temperature is sufficient to cause serious damage or even necrosis of tumor cells, which is suited to photothermal ablation of the tumor. As a control, the rise in temperature of the blank group (injected with only saline) and the SPA group is much lower than those of the *d*-PSPA group and the SPA + HRP group (Figure 6C), indicating that the existence of PSPA is the key to generating a photothermal effect at the tumor site. In addition, under the same conditions, the photothermal effect of the normal tissue *in situ* injected with SPA + HRP was also studied. It was observed that the surface temperature of normal tissue only increased by about 8°C under 1064 nm laser irradiation after 12 h of injection (Figure S20). These observations were in accordance with those obtained from the *in vivo* PA image (Figures 5B and S16). It indicated that PSPA could be *in situ* produced via the polymerization of SPA at the tumor site through the utilization of HRP to catalyze H_2O_2 overexpressed in the TME, and the further irradiation of this PSPA could generate heat. Such *in situ* polymerization of SPA to produce PSPA has significant photothermal specificity under laser irradiation in NIR-II region, which would avoid damage to normal tissues due to nonspecific overheating, providing the possibility of realization of tumor-specific PTT.

After confirming that SPA can be *in situ* polymerized into PSPA at the tumor site and the as-formed PSPA has benign photothermal conversion capability *in vivo*, *in vivo* PTT efficacy was further evaluated. Different groups were randomly divided by female Balb/c nude mice with 4T1 tumors, with intratumoral injection of saline, SPA, *d*-PSPA, and SPA +

HRP plus 1064 nm laser irradiation (1.0 W cm^{-2}) for 5 min. The tumors in the test groups (*d*-PSPA + Laser and SPA + HRP + Laser) shrink over the whole experimental period, and the tumors were almost eliminated on the 14th day (Figure 6D and E). In remarkable contrast, rapid growth of tumors was found for the control (injection of SPA, *d*-PSPA, or SPA + HRP, but without irradiation) and blank groups (only injection of saline or saline + laser irradiation) over time (Figure 6D). These *in vivo* results indicated that only injection of *d*-PSPA or SPA + HRP or only laser irradiation could not effectively inhibit tumor development. When considering that comparable PTT efficacy was observed for the *d*-PSPA + Laser and SPA + HRP + Laser groups, we could infer that the PTT effect of the SPA + HRP + Laser group was generated from NIR-II light mediated heating of *in situ* synthesized PSPA, in accordance with the results obtained from *in vivo* PA and thermal images (Figures 5B and 6B). As an essential parameter to evaluate the potential *in vivo* toxicity of materials, fluctuation in body weight of the tested mice was monitored. No obvious fluctuation in body weight was found over the whole experimental period (Figure 6F), and this illustrated that there were insignificant signs of toxic effects for such PTT process. Next, hematoxylin and eosin (H&E) staining of tumors was carried out. The tumor tissues in the test groups showed significant cellular damage, including irregular cell shrinkage and loss of contact, whereas the tumor tissues in the control and blank groups almost displayed insignificant cellular damage (Figure 7). These observations agreed well with the *in vivo* antitumor activities in which tumors treated with *d*-PSPA + Laser and SPA + HRP + Laser were seriously destroyed. Moreover, H&E staining of major organs (heart, liver, spleen, lung, kidney) did not exhibit any abnormality after 14-day treatments (Figure S21), demonstrating negligible systemic toxicity of those treatments. Overall, *in vitro* and *in vivo* experimental results demonstrated that the *in situ* polymerization of SPA into PSPA through the utilization of HRP to catalyze H_2O_2 is a highly effective and feasible approach to achieve tumor-specific phototheranostics.

4. CONCLUSIONS

In summary, we successfully developed one kind of aniline derivative (SPA) to polymerize into water-soluble polyaniline derivative (PSPA) through the utilization of HRP to catalyze H_2O_2 for generating $\bullet\text{OH}$. Based on this specific reaction, H_2O_2 overexpressed in the TME can be used for initiating *in situ* polymerization of SPA into PSPA at the tumor site. Benefiting from outstanding NIR-II absorption characteristics

of PSPA, this *in situ* polymerization can be validly monitored by PA signal at the NIR-II region. Meanwhile, *in situ* polymerization induced the size of polymeric materials from small to large, improving the distribution and retention of PSPA at tumor site. On the combination of NIR-II absorption of PSPA and the size variation induced by polymerization, such polymerization offered the possibility to realize tumor-specific NIR-II light mediated PA image and PTT of tumors, enhancing the precision and efficacy of tumor theranostics. As expected, tumor-specific phototheranostics was proved by *in vitro* and *in vivo* experimental data, where tumor-specific inhibition upon 1064 nm laser irradiation as well as real-time PA image at 1065 nm were realized. It should be mentioned that the integration of SPA and HRP into one system have not been carried out in this work, restricting systematic administration of SPA and HRP to conduct *in situ* polymerization. When considering that systematic administration is favored for clinical use, we will attempt to develop tumor-targeted nanoplatfoms with coloadng SPA and HRP to realize *in situ* polymerization via systematic administration in the follow-up work.

This work proposes novel biosynthesis of polyaniline derivatives at the tumor site via TME characteristics with the overexpression of H₂O₂ to activate *in situ* polymerization of aniline derivative and demonstrates that such *in situ* polymerization can be used for tumor-specific phototheranostics. In particular, it paves a new pathway to *in situ* biosynthesize other conjugated polymers by the utilization of TME characteristics for overcoming formidable challenges in tumor theranostics.

■ ASSOCIATED CONTENT

SI Supporting Information

The Supporting Information is available free of charge at <https://pubs.acs.org/doi/10.1021/acsami.2c19927>.

Water solubility, particle size, photothermal imaging, and other data (PDF)

■ AUTHOR INFORMATION

Corresponding Author

Bang-Ping Jiang – State Key Laboratory for Chemistry and Molecular Engineering of Medicinal Resources, Key Laboratory for Chemistry and Molecular Engineering of Medicinal Resources (Ministry of Education of China), Collaborative Innovation Center for Guangxi Ethnic Medicine, School of Chemistry and Pharmaceutical Sciences, Guangxi Normal University, Guilin 541004, P. R. China; orcid.org/0000-0002-0380-1618; Email: jiangbangping@mailbox.gxnu.edu.cn

Authors

Aihui Wang – State Key Laboratory for Chemistry and Molecular Engineering of Medicinal Resources, Key Laboratory for Chemistry and Molecular Engineering of Medicinal Resources (Ministry of Education of China), Collaborative Innovation Center for Guangxi Ethnic Medicine, School of Chemistry and Pharmaceutical Sciences, Guangxi Normal University, Guilin 541004, P. R. China

Hongyan Li – State Key Laboratory for Chemistry and Molecular Engineering of Medicinal Resources, Key Laboratory for Chemistry and Molecular Engineering of Medicinal Resources (Ministry of Education of China), Collaborative Innovation Center for Guangxi Ethnic

Medicine, School of Chemistry and Pharmaceutical Sciences, Guangxi Normal University, Guilin 541004, P. R. China

Hao Feng – State Key Laboratory for Chemistry and Molecular Engineering of Medicinal Resources, Key Laboratory for Chemistry and Molecular Engineering of Medicinal Resources (Ministry of Education of China), Collaborative Innovation Center for Guangxi Ethnic Medicine, School of Chemistry and Pharmaceutical Sciences, Guangxi Normal University, Guilin 541004, P. R. China

Huimin Qiu – State Key Laboratory for Chemistry and Molecular Engineering of Medicinal Resources, Key Laboratory for Chemistry and Molecular Engineering of Medicinal Resources (Ministry of Education of China), Collaborative Innovation Center for Guangxi Ethnic Medicine, School of Chemistry and Pharmaceutical Sciences, Guangxi Normal University, Guilin 541004, P. R. China

Rimei Huang – State Key Laboratory for Chemistry and Molecular Engineering of Medicinal Resources, Key Laboratory for Chemistry and Molecular Engineering of Medicinal Resources (Ministry of Education of China), Collaborative Innovation Center for Guangxi Ethnic Medicine, School of Chemistry and Pharmaceutical Sciences, Guangxi Normal University, Guilin 541004, P. R. China

Yiqin Wang – State Key Laboratory for Chemistry and Molecular Engineering of Medicinal Resources, Key Laboratory for Chemistry and Molecular Engineering of Medicinal Resources (Ministry of Education of China), Collaborative Innovation Center for Guangxi Ethnic Medicine, School of Chemistry and Pharmaceutical Sciences, Guangxi Normal University, Guilin 541004, P. R. China

Shichen Ji – State Key Laboratory for Chemistry and Molecular Engineering of Medicinal Resources, Key Laboratory for Chemistry and Molecular Engineering of Medicinal Resources (Ministry of Education of China), Collaborative Innovation Center for Guangxi Ethnic Medicine, School of Chemistry and Pharmaceutical Sciences, Guangxi Normal University, Guilin 541004, P. R. China; orcid.org/0000-0002-6322-7566

Hong Liang – State Key Laboratory for Chemistry and Molecular Engineering of Medicinal Resources, Key Laboratory for Chemistry and Molecular Engineering of Medicinal Resources (Ministry of Education of China), Collaborative Innovation Center for Guangxi Ethnic Medicine, School of Chemistry and Pharmaceutical Sciences, Guangxi Normal University, Guilin 541004, P. R. China

Xing-Can Shen – State Key Laboratory for Chemistry and Molecular Engineering of Medicinal Resources, Key Laboratory for Chemistry and Molecular Engineering of Medicinal Resources (Ministry of Education of China), Collaborative Innovation Center for Guangxi Ethnic Medicine, School of Chemistry and Pharmaceutical Sciences, Guangxi Normal University, Guilin 541004, P. R. China; orcid.org/0000-0002-7116-6919

Complete contact information is available at: <https://pubs.acs.org/doi/10.1021/acsami.2c19927>

Author Contributions

[†]A.W., H.L., and H.F. contributed equally to this work. B.P.J. and X.C.S. conceived the study. A.W. and H.L. conducted the main part of the experiments. H.F. participated in analyzing the experimental results and drew the schematic 1. H.Q. and R.H. wrote the draft. Y.W., S.J., and H.L. revised the manuscript. All

authors discussed the results and commented on the manuscript.

Notes

The authors declare no competing financial interest.

ACKNOWLEDGMENTS

This work was supported by the National Natural Science Foundation of China (22265004, 21977022, 21671046), and Natural Science Foundation of Guangxi (2018GXNSFFA281004, 2017GXNSFGA198004, and AD17129007) for financial support.

REFERENCES

- (1) Muir, V. G.; Burdick, J. A. Chemically Modified Biopolymers for the Formation of Biomedical Hydrogels. *Chem. Rev.* **2021**, *121*, 10908–10949.
- (2) Wang, X.; Li, M.; Hou, Y.; Li, Y.; Yao, X.; Xue, C.; Fei, Y.; Xiang, Y.; Cai, K.; Zhao, Y.; Luo, Z. Tumor-Microenvironment-Activated *in Situ* Self-Assembly of Sequentially Responsive Biopolymer for Targeted Photodynamic Therapy. *Adv. Funct. Mater.* **2020**, *30*, 2000229.
- (3) Stavrinidou, E.; Gabriellsson, R.; Nilsson, K. P. R.; Singh, S. K.; Franco-Gonzalez, J. F.; Volkov, A. V.; Jonsson, M. P.; Grimoldi, A.; Elgland, M.; Zozoulenko, I. V.; Simon, D. T.; Berggren, M. *In Vivo* Polymerization and Manufacturing of Wires and Supercapacitors in Plants. *Proc. Natl. Acad. Sci. U.S.A.* **2017**, *114*, 2807–2812.
- (4) Stavrinidou, E.; Gabriellsson, R.; Gomez, E.; Crispin, X.; Nilsson, O.; Simon, D. T.; Berggren, M. Electronic Plants. *Sci. Adv.* **2015**, *1*, e1501136.
- (5) Parker, D.; Daguette, Y.; Dufil, G.; Mantione, D.; Solano, E.; Cloutet, E.; Hadziioannou, G.; Näsholm, T.; Berggren, M.; Pavlopoulou, E.; Stavrinidou, E. Biohybrid Plants with Electronic Roots via *in Vivo* Polymerization of Conjugated Oligomers. *Mater. Horiz.* **2021**, *8*, 3295–3305.
- (6) Tommasini, G.; Dufil, G.; Fardella, F.; Strakosas, X.; Fergola, E.; Abrahamsson, T.; Bliman, D.; Olsson, R.; Berggren, M.; Tino, A.; Stavrinidou, E.; Tortiglione, C. Seamless Integration of Bioelectronic Interface in an Animal Model via *in Vivo* Polymerization of Conjugated Oligomers. *Bioact. Mater.* **2022**, *10*, 107–116.
- (7) Dufil, G.; Parker, D.; Gerasimov, J. Y.; Nguyen, T. Q.; Berggren, M.; Stavrinidou, E. Enzyme-Assisted *in Vivo* Polymerisation of Conjugated Oligomer Based Conductors. *J. Mater. Chem. B* **2020**, *8*, 4221–4227.
- (8) Mantione, D.; Istif, E.; Dufil, G.; Vallan, L.; Parker, D.; Brochon, C.; Cloutet, E.; Hadziioannou, G.; Berggren, M.; Stavrinidou, E.; Pavlopoulou, E. Thiophene-Based Trimers for *in Vivo* Electronic Functionalization of Tissues. *ACS Appl. Electron. Mater.* **2020**, *2*, 4065–4071.
- (9) Pham, J.; Forget, A.; Bridonneau, N.; Mattana, G.; Stavrinidou, E.; Zrig, S.; Piro, B.; Noel, V. *In Vivo* Electrochemically-Assisted Polymerization of Conjugated Functionalized Terthiophenes Inside the Vascular System of a Plant. *Electrochem. Commun.* **2022**, *137*, 107270.
- (10) Zhang, S.; Chen, H.; Wang, L.; Qin, X.; Jiang, B. P.; Ji, S. C.; Shen, X. C.; Liang, H. A General Approach to Design Dual Ratiometric Fluorescent and Photoacoustic Probes for Quantitatively Visualizing Tumor Hypoxia Levels *in Vivo*. *Angew. Chem., Int. Ed.* **2022**, *61*, e202107076.
- (11) Qiu, M.; Chen, J.; Huang, X.; Li, B.; Zhang, S.; Liu, P.; Wang, Q.; Qian, Z. R.; Pan, Y.; Chen, Y.; Zhao, J. Engineering Chemotherapeutic-Augmented Calcium Phosphate Nanoparticles for Treatment of Intraperitoneal Disseminated Ovarian Cancer. *ACS Appl. Mater. Interfaces.* **2022**, *14*, 21954–21965.
- (12) Dutta, A. K.; Alberge, J. B.; Sklavenitis-Pistofidis, R.; Lightbody, E. D.; Getz, G.; Ghobrial, I. M. Single-Cell Profiling of Tumour Evolution in Multiple Myeloma-Opportunities for Precision Medicine. *Nat. Rev. Clin. Oncol.* **2022**, *19*, 223–236.
- (13) Dai, Y.; Xu, C.; Sun, X.; Chen, X. Nanoparticle Design Strategies for Enhanced Anticancer Therapy by Exploiting the Tumour Microenvironment. *Chem. Soc. Rev.* **2017**, *46*, 3830–3852.
- (14) Zhong, X.; Wang, X.; Li, J.; Hu, J.; Cheng, L.; Yang, X. ROS-Based Dynamic Therapy Synergy with Modulating Tumor Cell-Microenvironment Mediated by Inorganic Nanomedicine. *Coord. Chem. Rev.* **2021**, *437*, 213828.
- (15) Chen, Z.; Wu, Y.; Yao, Z.; Su, J.; Wang, Z.; Xia, H.; Liu, S. 2D Copper(II) Metalated Metal-Organic Framework Nanocomplexes for Dual-Enhanced Photodynamic Therapy and Amplified Antitumor Immunity. *ACS Appl. Mater. Interfaces.* **2022**, *14*, 44199–44210.
- (16) Xiong, Y.; Xiao, C.; Li, Z.; Yang, X. Engineering Nanomedicine for Glutathione Depletion-Augmented Cancer Therapy. *Chem. Soc. Rev.* **2021**, *50*, 6013–6041.
- (17) Chang, J.; Qin, X.; Li, S.; He, F.; Gai, S.; Ding, H.; Yang, P. Combining Cobalt Ferrite Nanozymes with a Natural Enzyme to Reshape the Tumor Microenvironment for Boosted Cascade Enzyme-Like Activities. *ACS Appl. Mater. Interfaces.* **2022**, *14*, 45217–45228.
- (18) Wang, S.; Zhang, L.; Zhao, J.; He, M.; Huang, Y.; Zhao, S. A Tumor Microenvironment-Induced Absorption Red-Shifted Polymer Nanoparticle for Simultaneously Activated Photoacoustic Imaging and Photothermal Therapy. *Sci. Adv.* **2021**, *7*, eabe3588.
- (19) Dai, L.; Li, X.; Duan, X.; Li, M.; Niu, P.; Xu, H.; Cai, K.; Yang, H. A pH/ROS Cascade-Responsive Charge-Reversal Nanosystem with Self-Amplified Drug Release for Synergistic Oxidation-Chemotherapy. *Adv. Sci.* **2019**, *6*, 1801807.
- (20) Dai, L.; Li, X.; Zheng, X.; Fu, Z.; Yao, M.; Meng, S.; Zhang, J.; Han, B.; Gao, Q.; Chang, J.; Cai, K.; Yang, H. TGF- β Blockade-Improved Chemo-Immunotherapy with pH/ROS Cascade-Responsive Micelle via Tumor Microenvironment Remodeling. *Biomaterials* **2021**, *276*, 121010.
- (21) Fan, G.; Graham, A. J.; Kolli, J.; Lynd, N. A.; Keitz, B. K. Aerobic Radical Polymerization Mediated by Microbial Metabolism. *Nat. Chem.* **2020**, *12*, 638–646.
- (22) Zhou, Z.; Liang, H.; Yang, R.; Yang, Y.; Dong, J.; Di, Y.; Sun, M. Glutathione Depletion-Induced Activation of Dimersomes for Potentiating the Ferroptosis and Immunotherapy of “Cold” Tumor. *Angew. Chem., Int. Ed.* **2022**, *61*, e202202843.
- (23) Chen, T.; Huang, R.; Liang, J.; Zhou, B.; Guo, X. L.; Shen, X. C.; Jiang, B. P. Natural Polyphenol-Vanadium Oxide Nanozymes for Synergistic Chemodynamic/Photothermal Therapy. *Chem.—Eur. J.* **2020**, *26*, 15159–15169.
- (24) Gu, D.; Qiao, Y.; Fu, H.; Zhao, H.; Yue, X.; Wang, S.; Yin, Y.; Xi, R.; Fu, X.; Zhao, X.; Meng, M. Size-Controllable DNA Origami-Stacked Gold Nanoparticles for Deep Tumor-Penetrating Therapy. *ACS Appl. Mater. Interfaces.* **2022**, *14*, 38048–38055.
- (25) Zhang, Y.; Zhang, X.; Yang, H.; Yu, L.; Xu, Y.; Sharma, A.; Yin, P.; Li, X.; Kim, J. S.; Sun, Y. Advanced Biotechnology-Assisted Precise Sonodynamic Therapy. *Chem. Soc. Rev.* **2021**, *50*, 11227–11248.
- (26) Jaymand, M. Recent Progress in Chemical Modification of Polyaniline. *Prog. Polym. Sci.* **2013**, *38*, 1287–1306.
- (27) MacFarlane, L. R.; Shaikh, H.; Garcia-Hernandez, J. D.; Vespa, M.; Fukui, T.; Manners, I. Functional Nanoparticles Through π -Conjugated Polymer Self-Assembly. *Nat. Rev. Mater.* **2021**, *6*, 7–26.
- (28) Jiang, B. P.; Zhang, L.; Guo, X. L.; Shen, X. C.; Wang, Y.; Zhu, Y.; Liang, H. Poly(N-phenylglycine)-Based Nanoparticles as Highly Effective and Targeted Near-Infrared Photothermal Therapy/Photodynamic Therapeutic Agents for Malignant Melanoma. *Small* **2017**, *13*, 1602496.
- (29) Ruan, C.; Liu, C.; Hu, H.; Guo, X. L.; Jiang, B. P.; Liang, H.; Shen, X. C. NIR-II Light-Modulated Thermosensitive Hydrogel for Light-Triggered Cisplatin Release and Repeatable Chemo-Photothermal Therapy. *Chem. Sci.* **2019**, *10*, 4699–4706.
- (30) Liu, J.; Kim, Y. S.; Richardson, C. E.; Tom, A.; Ramakrishnan, C.; Birey, F.; Katsumata, T.; Chen, S.; Wang, C.; Wang, X.; Joubert, L. M.; Jiang, Y.; Wang, H.; Fenno, L. E.; Tok, J. B. H.; Pasca, S. P.; Shen, K.; Bao, Z.; Deisseroth, K. Genetically Targeted Chemical Assembly of Functional Materials in Living Cells, Tissues, and Animals. *Science* **2020**, *367*, 1372–1736.

- (31) Nothing, M. D.; Cao, H.; McKenzie, T. G.; Hocking, D. M.; Strugnell, R. A.; Qiao, G. G. Bacterial Redox Potential Powers Controlled Radical Polymerization. *J. Am. Chem. Soc.* **2021**, *143*, 286–293.
- (32) Wang, A.; Fan, G.; Qi, H.; Li, H.; Pang, C.; Zhu, Z.; Ji, S.; Liang, H.; Jiang, B. P.; Shen, X. C. H₂O₂-Activated *in Situ* Polymerization of Aniline Derivative in Hydrogel for Real-Time Monitoring and Inhibition of Wound Bacterial Infection. *Biomaterials* **2022**, *289*, 121798.
- (33) Geng, J.; Li, W.; Zhang, Y.; Thottappillil, N.; Clavadetscher, J.; Lilienkamp, A.; Bradley, M. Radical Polymerization Inside Living Cells. *Nat. Chem.* **2019**, *11*, 578–586.
- (34) Carregal-Romero, S.; Miguel-Coello, A. B.; Martínez-Parra, L.; Martí-Mateo, Y.; Hernansanz-Agustín, P.; Fernández-Afonso, Y.; Plaza-García, S.; Gutiérrez, L.; Muñoz-Hernández, M. M.; Carrillo-Romero, J.; Piñol-Cancer, M.; Lecante, P.; Blasco-Iturri, Z.; Fadón, L.; Almansa-García, A. C.; Möller, M.; Otaegui, D.; Enríquez, J. A.; Groult, H.; Ruiz-Cabello, J. Ultrasmall Manganese Ferrites for *in Vivo* Catalase Mimicking Activity and Multimodal Bioimaging. *Small* **2022**, *18*, 2106570.
- (35) Asif, M.; Aziz, A.; Ashraf, G.; Iftikhar, T.; Sun, Y.; Xiao, F.; Liu, H. Unveiling Microbiologically Influenced Corrosion Engineering to Transfigure Damages into Benefits: A Textile Sensor for H₂O₂ Detection in Clinical Cancer Tissues. *Chem. Eng. J.* **2022**, *427*, 131398.
- (36) Sahu, A.; Kwon, I.; Tae, G. Improving Cancer Therapy Through the Nanomaterials-Assisted Alleviation of Hypoxia. *Biomaterials* **2020**, *228*, 119578.
- (37) Wang, X.; Zhong, X.; Bai, L.; Xu, J.; Gong, F.; Dong, Z.; Yang, Z.; Zeng, Z.; Liu, Z.; Cheng, L. Ultrafine Titanium Monoxide (TiO_{1+x}) Nanorods for Enhanced Sonodynamic Therapy. *J. Am. Chem. Soc.* **2020**, *142*, 6527–6537.
- (38) Zhou, G.; Li, M. Near-Infrared-II Plasmonic Trienzyme-Integrated Metal-Organic Frameworks with High-Efficiency Enzyme Cascades for Synergistic Trimodal Oncotherapy. *Adv. Mater.* **2022**, *34*, 2200871.
- (39) Kospa, D. A.; Ahmed, A. I.; Samra, S. E.; El-Hakam, S. A.; Ibrahim, A. A. Flexible CuO-rGO/PANI Thermal Absorber with High Broadband Photoresponse and Salt Resistance for Efficient Desalination of Oil-Contaminated Seawater. *Desalination* **2022**, *528*, 115612.
- (40) Wu, J.; Zhang, Y.; Jiang, K.; Wang, X.; Blum, N. T.; Zhang, J.; Jiang, S.; Lin, J.; Huang, P. Enzyme-Engineered Conjugated Polymer Nanoplatfor for Activatable Companion Diagnostics and Multistage Augmented Synergistic Therapy. *Adv. Mater.* **2022**, *34*, 2200062.
- (41) Antony, M. J.; Jayakannan, M. Polyaniline Nanoscaffolds for Colorimetric Sensing of Biomolecules via Electron Transfer Process. *Langmuir* **2011**, *27*, 6268–6278.
- (42) Huang, H.; Zeng, X.; Li, W.; Wang, H.; Wang, Q.; Yang, Y. Reinforced Conducting Hydrogels Prepared from the *in Situ* Polymerization of Aniline in an Aqueous Solution of Sodium Alginate. *J. Mater. Chem. A* **2014**, *2*, 16516.
- (43) Chen, Z.; Mei, S.; Li, W.; Xu, N.; Dong, Y.; Jin, Y.; Ouyang, M.; Zhang, C. Study of Multi-Electron Redox Mechanism via Electrochromic Behavior in Hexaazatrinaphthylene-Based Polymer as the Cathode of Lithium-Organic Batteries. *J. Mater. Chem. A* **2021**, *9*, 27010–27018.
- (44) Jiang, B. P.; Zhang, L.; Zhu, Y.; Shen, X. C.; Tan, X. Y.; Cheng, L.; Liang, H. Water-Soluble Hyaluronic Acid-Hybridized Polyaniline Nanoparticles for Effectively Targeted Photothermal Therapy. *J. Mater. Chem. B* **2015**, *3*, 3767–3776.
- (45) Wang, C.; Li, Y.; Yu, H. Y.; Abdalkarim, H. S. Y.; Zhou, J.; Yao, J.; Zhang, L. Continuous Meter-Scale Wet-Spinning of Cornlike Composite Fibers for Eco-Friendly Multifunctional Electronics. *ACS Appl. Mater. Interfaces* **2021**, *13*, 40953–40963.
- (46) Youssef, A. M.; El-Samahy, M. A.; Abdel Rehim, M. H. Preparation of Conductive Paper Composites Based on Natural Cellulosic Fibers for Packaging Applications. *Carbohydr. Polym.* **2012**, *89*, 1027–1032.
- (47) Wang, Y.; Yang, Y.; Yang, L.; Lin, Y.; Tian, Y.; Ni, Q.; Wang, S.; Ju, H.; Guo, J.; Lu, G. Gold Nanostar@Polyaniline Theranostic Agent with High Photothermal Conversion Efficiency for Photoacoustic Imaging-Guided Anticancer Phototherapy at a Low Dosage. *ACS Appl. Mater. Interfaces* **2022**, *14*, 28570–28580.
- (48) Lucero, M. Y.; East, A. K.; Reinhardt, C. J.; Sedgwick, A. C.; Su, S.; Lee, M. C.; Chan, J. Development of NIR-II Photoacoustic Probes Tailored for Deep-Tissue Sensing of Nitric Oxide. *J. Am. Chem. Soc.* **2021**, *143*, 7196–7202.
- (49) Wang, F.; Gourgues, R.; Baghdasaryan, A.; Zadeh, I. E.; Los, J. W. N.; Fognini, A. *In Vivo* Non-Invasive Confocal Fluorescence Imaging Beyond 1,700 nm Using Superconducting Nanowire Single-Photon Detectors. *Nat. Nanotechnol.* **2022**, *17*, 653–660.
- (50) Jia, T.; Chen, G. Lanthanide Nanoparticles for Near-Infrared II Theranostics. *Coord. Chem. Rev.* **2022**, *471*, 214724.
- (51) Liu, Y.; Li, Y.; Koo, S.; Sun, Y.; Liu, Y.; Pan, Y.; Zhang, Z.; Du, M.; Lu, S.; Qiao, X.; Gao, J.; Wang, X.; Deng, Z.; Meng, X.; Xiao, Y.; Kim, J. S.; Hong, X. Versatile Types of Inorganic/Organic NIR-IIa/IIb Fluorophores: From Strategic Design Toward Molecular Imaging and Theranostics. *Chem. Rev.* **2022**, *122*, 209–268.